

Bridging ocean wave physics and deep learning: Physics-informed neural operators for nonlinear wavefield reconstruction in real-time

Svenja Ehlers,¹ Merten Stender,² and Norbert Hoffmann^{1,3}

¹*Dynamics Group, Hamburg University of Technology, Germany*

²*Cyber-Physical Systems in Mechanical Engineering, Technische Universität Berlin, Germany*

³*Department of Mechanical Engineering, Imperial College London, United Kingdom*

(*Electronic mail: svenja.ehlers@tuhh.de)

(Dated: 6 August 2025)

Accurate real-time prediction of phase-resolved ocean wave fields remains a critical yet largely unsolved problem, primarily due to the absence of practical data assimilation methods for reconstructing initial conditions from sparse or indirect wave measurements. While recent advances in supervised deep learning have shown potential for this purpose, they require large labelled datasets of ground truth wave data, which are infeasible to obtain in real-world scenarios. To overcome this limitation, we propose a Physics-Informed Neural Operator (PINO) framework for reconstructing spatially and temporally phase-resolved, nonlinear ocean wave fields from sparse measurements, without the need for ground truth data during training. This is achieved by embedding residuals of the free surface boundary conditions of ocean gravity waves into the loss function of the PINO, constraining the solution space in a soft manner. After training, we validate our approach using highly realistic synthetic wave data and demonstrate the accurate reconstruction of nonlinear wave fields from both buoy time series and radar snapshots. Our results indicate that PINOs enable accurate, real-time reconstruction and generalize robustly across a wide range of wave conditions, thereby paving the way for operational, data-driven wave reconstruction and prediction in realistic marine environments.

I. INTRODUCTION

Real-time and phase-resolved wave prediction of nonlinear ocean surface waves has the potential to enhance the planning of offshore operations, optimizing wave energy converter control, and improve maritime safety. In this context, *phase-resolved* refers to the precise tracing of the wave evolution in space and time. *Real-time capability* requires wave computations to be faster than the physical waves, while modelling *nonlinearity* is crucial to capture key dynamics such as wave-wave interactions, nonlinear dispersion, and rogue waves. An important aspect of phase-resolved wave prediction is that, in practice, the initial conditions are typically not available. Wave fields are measured using in-situ (e.g. wave rider buoys) or remote sensing (e.g. radar systems) instruments, resulting in sparse measurement data. This first requires a reconstruction of the corresponding wave field from these measurements to initiate the actual wave prediction.

For intermediate to deep water, the nonlinear potential flow theory is commonly used to model surface gravity waves and can be solved with various numerical methods¹⁻⁴. The High-Order Spectral Method (HOSM)^{5,6} is popular for this purpose⁷⁻¹⁰, as with ongoing advancements in computational hardware, HOSM holds promise for highly accurate real-time predictions of nonlinear water waves¹¹⁻¹³. However, the fast and accurate reconstruction of the initial conditions, also known as wave data assimilation, remains a more difficult task^{13,14}: HOSM-assimilation methods follow either sequential^{15,16} or variational¹⁷⁻²¹ strategies, which may cause poor accuracy or require computationally expensive cost-function minimization. Moreover, these methods usually determine only the optimal initial surface elevation, whereas a full potential flow description requires both elevation and surface velocity potential²². To address this, Desmars et al.

(2023)²³ and Köllisch et al. (2018)¹³ integrate the free surface boundary conditions into their assimilation methods. Although the first method enables effective parallelization, its real-time capability is not demonstrated. While the second approach theoretically allows for real-time computations, it instead demands unrealistically high spatial and temporal resolution of measurement data²⁴.

In summary, the data assimilation problem for initializing nonlinear, phase-resolved, real-time wave prediction methods remains largely unresolved. Inspired by recent advances in artificial intelligence that have transformed various research domains, our previous work explored (physics-informed) machine learning approaches to address this challenge:

- In Ehlers et al. (2023)²⁵, we demonstrate that a Fourier Neural Operator (FNO) architecture²⁶ effectively reconstructs initial wave elevations from radar snapshots. Once trained, the FNO generalizes this mapping across diverse wave conditions and enables real-time applications. However, its supervised training approach requires a large dataset of ground truth wave elevations for training. While radar measurements are available in real-world settings, acquiring high-resolution ground truth wave elevation data would necessitate an impractically dense network of buoys. Therefore, the FNO-approach relies on synthetic wave and radar data and cannot be retrained using real-world data.
- In Ehlers et al. (2025)²⁷, we address the unavailability of ground truth wave data by utilizing a Physics-Informed Neural Network (PINN)²⁸. Unlike the FNO-approach, the PINN infers high-resolution spatio-temporal wave elevations and velocity potentials directly from sparse measurement data, without access to a ground truth. The physical consistency of these reconstructed wave surfaces is ensured by incorporating the potential flow equations into the loss function. However, PINNs require direct measurements

of the physical quantities defining the solution. This implies, PINNs can assimilate wave surfaces from buoy measurements, but not from indirect observations such as radar backscatter intensities. Moreover, PINNs lack generalization across wave conditions and solve an individual inverse problem for each wave instance, causing high computational costs that limit their applicability in real-time scenarios.

Also, ML-based approaches for modelling phase-resolved wave dynamics proposed by other research groups^{29–32} have also not yet resolved these challenges: Trained using only one or a few specific sea states, they are prone to poor generalization. Moreover, these methods map wave time-series to time-series at fixed spatial points, preventing extrapolation of wave information to untrained locations. This implies the methods can be considered temporally phase-resolved but not spatially. While more advanced ML methods^{33,34} can represent spatio-temporal wave dynamics, they assume fully resolved initial conditions, which is impractical for real-world scenarios.

Therefore, we aim to advance the reconstruction of initial wave fields from sparse measurements by combining the strengths of our FNO-based²⁵ and PINN-based²⁷ approach, leveraging the concept of Physics-Informed Neural Operators (PINOs) proposed by Li et al. (2024)³⁵. PINOs are a variation of neural operators that incorporate physical laws into their loss functions to overcome the limitations of purely physics-based and purely data-driven methods. The approach has been validated on PDE benchmarks³⁶ and applied e.g. to fluid dynamics³⁷, acoustics³⁸, or chaotic system dynamics³⁹. With the PINO acting as an universal approximator for a nonlinear solution operator⁴⁰, we hypothesize that the PINO-based wave reconstruction approach developed in this work

- (H1) reconstructs spatially and temporally phase-resolved, nonlinear wave surfaces from (a) sparse buoy time-series or (b) radar snapshot measurements
- (H2) eliminates the need for ground truth data during training, enabling learning from real-world data
- (H3) allows for rapid wave surface reconstruction, supporting real-time forecasting applications
- (H4) generalizes its reconstruction ability for a broad range of wave conditions

To validate these hypotheses, Sec. II introduces the high-order spectral method used to generate realistic wave reference data, followed by wave measurement techniques and a description of the PINO architecture and training procedure. The PINO approach is evaluated in Sec. III A for reconstructing wave surface elevations from buoy time-series measurements, and in Sec III B for reconstruction from radar intensity snapshots, using only a single time-series measurement for calibration. Finally, Sec. IV summarizes the results and discusses the potential for operational deployment of the PINO approach.

II. METHODS

This section first introduces the High-order spectral method used to generate synthetic wave elevation and surface poten-

tial data that are used as reference only to compare the PINO reconstructions post-training. Next, we describe how we generate sparse buoy or radar measurements intended as the input. The PINO architecture tailored to the assimilation problem and its training procedure are explained in the last subsection.

A. Potential flow theory and high-order spectral method

In the modelling of nonlinear, non-breaking ocean gravity waves, the problem is typically formulated within the framework of potential flow theory. Assuming an inviscid and irrotational fluid, the flow field is described by a velocity potential $\Phi(x, z, t)$ in the fluid volume and a surface elevation $\eta(x, t)$, governed by the Laplace equation, a kinematic and dynamic surface boundary condition and the bottom boundary at depth d . Solving this system of equations analytically is challenging, such that numerical methods are used to approximate solutions. The High-Order Spectral Method (HOSM)^{5,6} has proven particularly efficient and accurate for that purpose^{11,41}.

The HOSM first introduces a surface velocity potential $\Phi^s(x, t) = \Phi(x, \eta(x, t), t)$, which allows us to convert the potential flow problem from the fluid domain to free surface quantities by rewriting it in the form of Zakharov⁴²

$$\eta_t + \eta_x \Phi_x^s - W \left(1 + (\eta_x)^2 \right) = 0 \quad \text{on } z = \eta(x, t) \quad (1)$$

$$\Phi_t^s + g\eta + \frac{1}{2} (\Phi_x^s)^2 - \frac{1}{2} W^2 \left(1 + (\eta_x)^2 \right) = 0 \quad \text{on } z = \eta(x, t). \quad (2)$$

For these free surface boundary conditions (FSBC) and initial values of η and Φ^s , numerical integration in time can be performed, with the vertical velocity on the free surface $W = \Phi_z|_{z=\eta(x,t)}$ being the only unknown remaining. To solve for W , the HOSM expresses the velocity potential and vertical velocity as perturbation series in wave steepness

$$\Phi(x, z, t) = \sum_{m=1}^M \Phi^{(m)}(x, z, t) \quad (3)$$

$$W(x, t) = \sum_{m=1}^M W^{(m)}(x, t) \quad (4)$$

up to a predefined order of nonlinearity M . This allows expansion of each $\Phi^{(m)}$ and $W^{(m)}$ as a Taylor series around the mean free surface. Separating the terms of each order (m) yields

$$\Phi^{(1)}(x, 0, t) = \Phi^s(x, t) \quad (5)$$

$$\Phi^{(m)}(x, 0, t) = - \sum_{\ell=1}^{m-1} \frac{\eta^\ell}{\ell!} \frac{\partial^\ell \Phi^{(m-\ell)}}{\partial z^\ell} \Big|_{z=0} \quad (6)$$

for the perturbation potentials. The terms of the vertical velocity are obtained by a further derivative in z -direction

$$W^{(m)}(x, t) = \sum_{\ell=0}^{m-1} \frac{\eta^\ell}{\ell!} \frac{\partial^{\ell+1} \Phi^{(m-\ell)}}{\partial z^{\ell+1}} \Big|_{z=0}. \quad (7)$$

Assuming periodic boundaries, the Fast Fourier Transform can be used to determine $\Phi^{(m)}$ and its spatial derivatives in Fourier space, while the nonlinear products are calculated in physical space. In most engineering applications, $M = 4$ is sufficient to capture all important nonlinear interactions^{24,43}.

B. Wave Measurements

Wave measurement systems can be broadly categorized into in-situ (e.g. wave rider buoys, acoustic and pressure sensors) and remote sensing (e.g. X-band radar, Lidar cameras) methods. This work focuses on buoy (case A) and X-Band radar measurements (case B) as input for wave reconstruction.

In-situ devices provide single-point measurements, which lack directional wavefield information, often necessitating an array of several devices^{11,14}. Instead, when desiring high spatial resolution, measurements are usually performed using remote sensors mounted on a structure. The antenna of an X-Band radar system rotates with a revolution time of usually 1 – 2s⁴⁴ while emitting radar beams that interact with the ocean surface, causing a backscatter to the antenna⁴⁵. This way, several square kilometres are monitored with a spatial resolution of approximately 4 – 10m⁴⁴. However, radar backscatter intensities ξ do not directly correlate with wave elevations η due to modulation mechanisms: Tilt modulation depends on the local incidence angle, which affects the radar's ability to detect backscatter based on the relative wave facet orientation. Shadowing modulation occurs when high waves prevent the radar beams from reaching waves behind, leading to zero-backscatter intensities^{46–48}.

Since real-world measurements lack ground truth wave elevation data for direct comparison, this study validates the PINO approach using synthetic data. To generate synthetic X-Band radar data from wave elevation surfaces, we use a geometric approach depicted in Fig. 1. Tilt modulation \mathcal{T} is modelled along a range r around the radar antenna and based on the local incidence angle $\tilde{\Theta}(r, t)$, defined between the normal vector $\mathbf{n}(r, t)$ of the illuminated wave facet $\eta(r, t)$ and the vector $\mathbf{u}(r, t)$ pointing toward the antenna as

$$\mathcal{T}(r, t) = c_1 \frac{\mathbf{n}(r, t) \mathbf{u}(r, t)}{|\mathbf{n}(r, t)| |\mathbf{u}(r, t)|} + c_2 \quad \text{if } |\tilde{\Theta}(r, t)| \leq \frac{\pi}{2} \quad (8)$$

whereas $|\cdot|$ is the Euclidean norm and c_1 and c_2 are scaling factors and offsets depending on the system calibration²³.

Shadowing modulation depends on the nominal incidence angle $\Theta(r, t) = \tan^{-1} \left[\frac{R(r)}{z_a - \eta(r, t)} \right]$, where $R(r)$ is the horizontal distance from the radar, and z_a is the antenna height. A wave $\eta(r, t)$ is shadowed if a closer wave $\eta(r', t)$ at $R(r') < R(r)$ satisfies $\Theta(r', t) \geq \Theta(r, t)$. The total radar backscatter intensity

$$\xi(r, t) = \begin{cases} 0 & \text{if } R(r') < R(r) \text{ and } \Theta(r', t) \geq \Theta(r, t) \\ \mathcal{T}(r, t) & \text{otherwise} \end{cases} \quad (9)$$

then is a combination of tilt and shadowing effects^{47,48}.

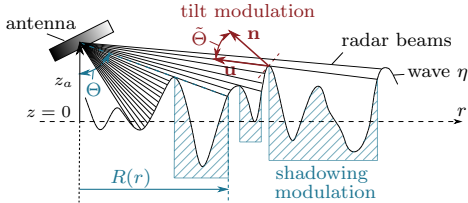


FIG. 1. Geometric representation of tilt and shadowing modulation.

C. Physics-informed neural operator

To address the limitations of our previous ML approaches for reconstructing initial wave fields from sparse measurements, we develop a Physics-Informed Neural Operator (PINO). Unlike a purely data-driven approach, the PINO training does not rely on minimizing the error between the network's reconstructions $\tilde{\eta} \in \mathbb{R}^{n_x \times n_t}$ and a high-resolution ground truth $\eta_{\text{true}} \in \mathbb{R}^{n_x \times n_t}$, as obtaining such spatio-temporal wave data as the ground truth is often impractical in real-world scenarios. Instead, the PINO leverages sparse measurements where available and accounts for the remaining domain by incorporating physics into its loss function.

1. Sensor data generation

While our PINO approach eliminates the need for fully resolved ground truth wave surfaces during training, such data remains valuable to validate the physical correctness of the reconstructions after training. Once validated, the PINO could be trained directly on real-world measurements. To enable this validation, we generate synthetic wave elevation surfaces η_{HOSM} and corresponding surface potentials Φ_{HOSM} using the HOSM described in Sec. II A. The initial elevations are sampled from a JONSWAP TMA spectrum^{49,50} with random phases, a peak enhancement factor $\gamma = 3.3$ and various combinations of peak wavelength $L_p \in \{100, 110, \dots, 200\}$ m and wave steepness $\varepsilon \in \{0.02, 0.03, \dots, 0.13\}$. A relaxation period of 20 peak periods precedes data collection to allow the development of nonlinear wave dynamics. The saved domain for η_{HOSM} and Φ_{HOSM} spans 1953 m with resolution $\Delta x = 3.906$ m ($n_x = 500$) and 100 s with resolution $\Delta t = 0.2$ s ($n_t = 500$), although the HOSM itself uses smaller time steps.

In total, 1056 wave surfaces $\eta_{\text{HOSM}} \in \mathbb{R}^{n_x \times n_t}$ and velocity potentials $\Phi_{\text{HOSM}}^s \in \mathbb{R}^{n_x \times n_t}$ are generated (eight samples per ε - L_p -combination). From these surfaces, $n_{\text{buoy}} = 5$ buoy measurements $\eta_m \in \mathbb{R}^{n_{\text{buoy}} \times n_t}$ are extracted as PINO input for Sec. III A (case A). For Sec. III B (case B) instead, radar snapshots are generated as input using Eqs. (8-9) with a radar rotation period of $\Delta t_r = 2.0$ s. Each sample then contains $n_{\text{snap}} = 50$ snapshots, is denoted as $\xi_m \in \mathbb{R}^{n_x \times n_{\text{snap}}}$, and is accompanied by a single buoy measurement $\eta_{\text{cal}} \in \mathbb{R}^{1 \times n_t}$, which serves for calibration but is not included as a direct input. The complete dataset is split into training, validation, and test sets at a ratio of 0.6 – 0.2 – 0.2, resulting in a relatively small number of 634 measurement samples for training. Although the PINO is solely trained on sparse measurements η_m or ξ_m , the original, fully-resolved HOSM data is split using the same ratio, enabling a comparison of the PINO's reconstruction ($\tilde{\eta}$ and $\tilde{\Phi}^s$) with a reference (η_{HOSM} and Φ_{HOSM}^s) after training.

2. PINO architecture and training

Our PINO architecture in Fig. 2 builds upon the strengths of the FNO²⁶, as learning features in Fourier space has proven effective for wave reconstruction²⁵. The model either takes

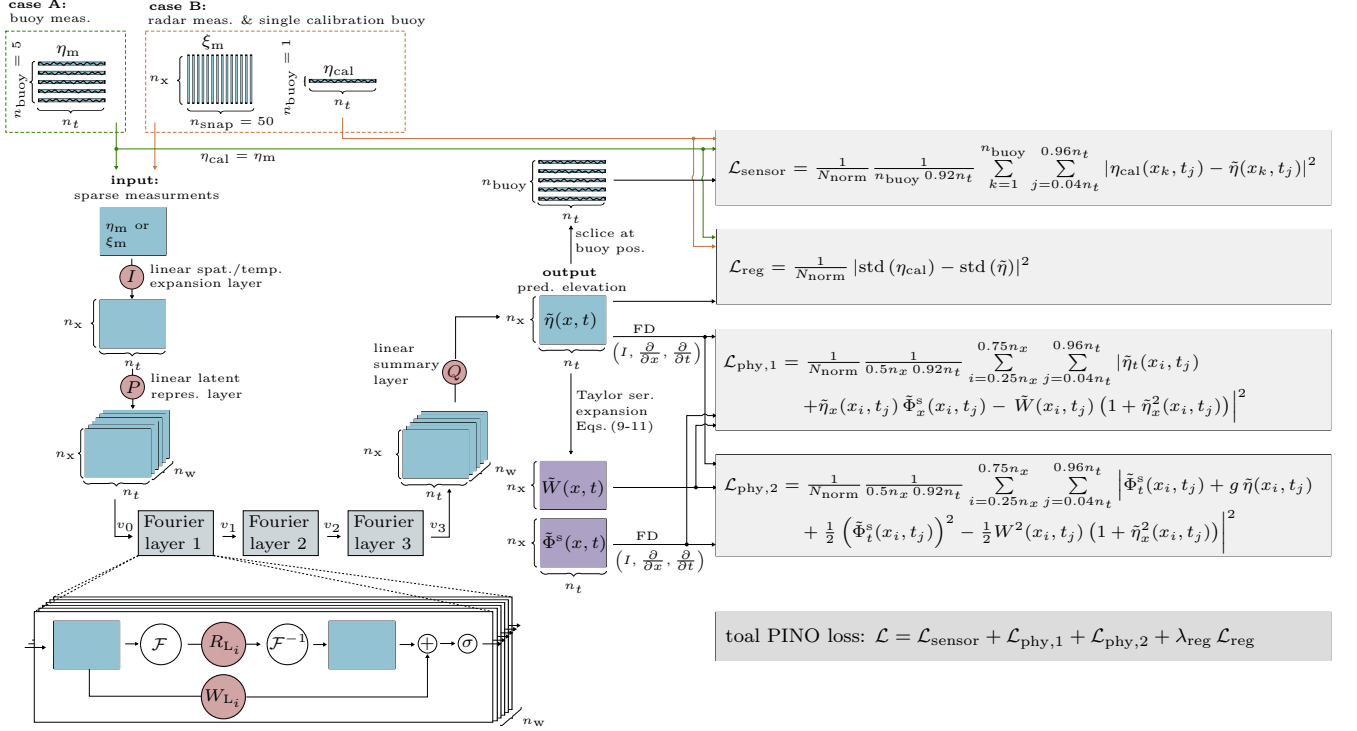


FIG. 2. Physics-informed neural operator (PINO) for reconstructing spatio-temporal wave elevation fields $\tilde{\eta}$ from sparse buoy η_m (case A) or radar ξ_m (case B) measurements. Each sparse input sample is lifted to a latent space by layers I and P , processed by n_F Fourier layers and projected to the target output dimension by layer Q . Due to the absence of ground truth data, training is guided by sensor consistency at the calibration buoy locations from the input ($\mathcal{L}_{\text{sensor}}$), physics-based losses from residuals of the free-surface boundary conditions ($\mathcal{L}_{\text{phy},1}$, $\mathcal{L}_{\text{phy},2}$), and a regularization term \mathcal{L}_{reg} promoting meaningful wave elevation in $\tilde{\eta}$. The required surface potential $\tilde{\Phi}^s$ and vertical velocity \tilde{W} for the physics-loss terms are approximated from $\tilde{\eta}$ via HOSM (Eq. 3-7), with spatial and temporal derivatives computed in Fourier space.

sparse buoy measurements $\eta_m \in \mathbb{R}^{n_{\text{buoy}} \times n_t}$ (case A) or radar snapshots $\xi_m \in \mathbb{R}^{n_x \times n_{\text{snap}}}$ (case B) as input and outputs high-resolution spatio-temporal wave elevations $\tilde{\eta} \in \mathbb{R}^{n_x \times n_t}$. Unlike standard FNOs, which have matching input and output dimensions, our PINO setup first requires dimension expansion via a linear layer I in space (case A) or time (case B). Another linear layer P then projects this expanded input into a latent representation $v_0 \in \mathbb{R}^{n_x \times n_t \times n_w}$ with n_w channels. To reduce boundary effects during the Fourier transform, v_0 is padded with 12 zero entries in both dimensions before entering the first Fourier layer.

Each Fourier layer operates on its input v_i via two complementary paths. The upper path applies a discrete Fourier transform \mathcal{F} to each channel, truncates to n_m modes, scales via a linear transformation R_{L_i} and then transforms back to the spatial domain via inverse Fourier transform \mathcal{F}^{-1} . The lower path applies a linear transformation W_{L_i} in the spatial domain to account for non-periodic boundaries and higher-order modes. The outputs of both paths are summed, passed through a GeLU activation σ , resulting in v_{i+1} for the next layer. After n_F Fourier layers, the zero-padding is removed and a final linear layer Q maps the latent representation to the output $\tilde{\eta} \in \mathbb{R}^{n_x \times n_t}$.

To generate meaningful wave surfaces $\tilde{\eta} \in \mathbb{R}^{n_x \times n_t}$ from measurements, the weights of the PINO layers (I , P , R_{L_i} ,

W_{L_i} , Q) are optimized by minimizing a loss function. In the absence of spatio-temporal ground truth data, alternative loss sources are required. One source is the sensor loss term $\mathcal{L}_{\text{sensor}}$, which compares the output $\tilde{\eta}$ to available buoy data. For case A, where buoy measurements $\eta_m \in \mathbb{R}^{5 \times n_t}$ serve as input, the reconstructed values $\tilde{\eta}_b \in \mathbb{R}^{5 \times n_t}$ are extracted from $\tilde{\eta}$ at buoy locations x_b and compared to the input $\eta_{\text{cal}} = \eta_m$. In case B, using radar snapshots as input, a single time series $\tilde{\eta}_b \in \mathbb{R}^{1 \times n_t}$ is extracted at the calibration buoy location and compared to $\eta_{\text{cal}} \in \mathbb{R}^{1 \times n_t}$. Next, to achieve physical consistency also between the buoy locations, we incorporate the residuals of the FSBCs (Eqs. 1-2) as physics-informed loss terms $\mathcal{L}_{\text{phy},1}$ and $\mathcal{L}_{\text{phy},2}$. These equations involve the surface velocity potential $\tilde{\Phi}^s \in \mathbb{R}^{n_x \times n_t}$ and vertical velocity $\tilde{W} \in \mathbb{R}^{n_x \times n_t}$ which are approximated from the predicted surface elevation $\tilde{\eta}$ using a fourth-order Taylor series expansion from the HOSM (Eqs. 3-7). The required spatial and temporal derivatives of $\tilde{\eta}$ and $\tilde{\Phi}^s$ are computed effectively using differentiation in the Fourier space (FD)²⁶. As the HOSM and FD inherently assume periodic boundaries - rarely present in real-world data - we apply Tukey windows along both axes when computing $\tilde{\Phi}^s$, \tilde{W} and derivatives to suppress spectral leakage. Therefore, loss terms are evaluated only over the central region ($i = n_x/4, \dots, 3n_x/4$ and $j = n_t/25, \dots, 24n_t/25$), while larger data structures are processed in the background. Finally, to avoid trivial solutions (e.g. $\tilde{\eta} = 0$ m, which satisfies

the physics losses), we introduce a regularization term \mathcal{L}_{reg} that compares the standard deviation (std) of the output field $\tilde{\eta}$ to that of the sparse calibration buoy η_{cal} , both only inside the region unaffected by the Tukey window. While not strictly necessary and weighted modestly by $\lambda_{\text{reg}} = 0.25$, the

term \mathcal{L}_{reg} promotes realistic variability in buoy-free regions, enhancing accuracy and convergence. In summary, the total loss

$$\mathcal{L} = \mathcal{L}_{\text{sensor}} + \mathcal{L}_{\text{phy},1} + \mathcal{L}_{\text{phy},2} + \lambda_{\text{reg}} \mathcal{L}_{\text{reg}} \quad (10)$$

then is composed of multiple components

$$\mathcal{L}_{\text{sensor}} = \frac{1}{N_{\text{norm}}} \frac{1}{n_{\text{buoy}} n_t} \sum_{k=1}^{n_{\text{buoy}}} \sum_{j=0.04n_t}^{0.96n_t} |\eta_{\text{cal}}(x_k, t_j) - \tilde{\eta}_{\text{b}}(x_k, t_j)|^2 \quad (11)$$

$$\mathcal{L}_{\text{phy},1} = \frac{1}{N_{\text{norm}}} \frac{1}{0.5n_x n_t} \sum_{i=0.25n_x}^{0.75n_x} \sum_{j=0.04n_t}^{0.96n_t} \left| \tilde{\eta}_l(x_i, t_j) + \tilde{\eta}_x(x_i, t_j) \tilde{\Phi}^s(x_i, t_j) - \tilde{W}(x_i, t_j) \left(1 + \tilde{\eta}_x^2(x_i, t_j) \right) \right|^2 \quad (12)$$

$$\mathcal{L}_{\text{phy},2} = \frac{1}{N_{\text{norm}}} \frac{1}{0.5n_x n_t} \sum_{i=0.25n_x}^{0.75n_x} \sum_{j=0.04n_t}^{0.96n_t} \left| \tilde{\Phi}_t^s(x_i, t_j) + g \tilde{\eta}(x_i, t_j) + \frac{1}{2} (\tilde{\Phi}_t^s(x_i, t_j))^2 + \frac{1}{2} \tilde{W}^2(x_i, t_j) \left(1 + \tilde{\eta}_x^2(x_i, t_j) \right) \right|^2 \quad (13)$$

$$\mathcal{L}_{\text{reg}} = \frac{1}{N_{\text{norm}}} |\text{std}(\eta_{\text{cal}}) - \text{std}(\tilde{\eta})|^2. \quad (14)$$

The sample-specific normalization factor

$$N_{\text{norm}} = \frac{1}{n_{\text{buoy}} n_t} \sum_{k=1}^{n_{\text{buoy}}} \sum_{j=0.04n_t}^{0.96n_t} |\eta_{\text{cal}}(x_k, t_j)|^2 \quad (15)$$

additionally prevents large-amplitude samples from disproportionately influencing the loss and biasing the training process. Moreover, although advanced adaptive loss weighing schemes exist^{51–54}, we found that empirical manual tuning of the loss weights is sufficient for demonstrating the usefulness of our PINO. Finally, the total loss (Eq. 10) is minimized using the AdamW optimizer^{55,56} with an initial learning rate of $lr = 0.001$, which is halved every 25 epochs. A batch size of 8 is used during training performed on a NVIDIA GeForce RTX 3090 GPU, with early stopping implemented after 50 epochs of no further improvement on the validation set.

3. Error metric

To evaluate the PINO's accuracy in reconstructing wave elevations or surface potentials after finishing the training, we employ the Surface Similarity Parameter (SSP)⁵⁷ as error metric. For two spatio-temporal surfaces, \mathbf{y}_{HOSM} (η_{HOSM} or Φ_{HOSM}^s) and $\tilde{\mathbf{y}}$ ($\tilde{\eta}$ or $\tilde{\Phi}^s$) the $\text{SSP} \in [0, 1]$ integrates deviations in phase, frequency and amplitude into a scalar measure by comparing their discrete Fourier transforms $F_{\mathbf{y}_{\text{HOSM}}}$ and $F_{\tilde{\mathbf{y}}}$ as

$$\text{SSP} = \frac{\sqrt{\int |F_{\mathbf{y}_{\text{HOSM}}}(\omega, k) - F_{\tilde{\mathbf{y}}}(\omega, k)|^2 d\omega dk}}{\sqrt{\int |F_{\mathbf{y}_{\text{HOSM}}}(\omega, k)|^2 d\omega dk} + \sqrt{\int |F_{\tilde{\mathbf{y}}}(\omega, k)|^2 d\omega dk}}. \quad (16)$$

Here, ω denotes the wave frequency and k the wavenumber vector. The SSP recently has been applied in research related to ocean wave dynamics^{23,25,27,34,58–60} due to the straightforward error assessment, with $\text{SSP} = 0$ indicating perfect alignment and $\text{SSP} = 1$ indicating phase-inverted signals or a comparison against zero.

III. RESULTS

The following sections present the results of training the PINO to reconstruct fully resolved wave surfaces $\tilde{\eta} \in \mathbb{R}^{n_x \times n_t}$ from sparse measurements. Sec. III A examines the reconstruction from buoy measurements $\eta_{\text{m}} \in \mathbb{R}^{n_{\text{buoy}} \times n_t}$, denoted as mapping $\mathcal{M}_A : \eta_{\text{m}} \rightarrow \tilde{\eta}$, while Sec. III B addresses reconstruction from radar snapshots $\xi_{\text{m}} \in \mathbb{R}^{n_x \times n_{\text{snap}}}$ as $\mathcal{M}_B : \xi_{\text{m}} \rightarrow \tilde{\eta}$. Both models are trained using the sparse input data only, without access to a ground truth. The relatively small training set contains 634 sparse buoy η_{m} (case A) or radar ξ_{m} (case B) samples generated according to Section II C 1. Performance is monitored on a validation set of 211 samples during training, and final evaluation is conducted in inference mode on an independent test set of another 211 samples.

A. Reconstruction from buoy measurements

Case A in Fig. 2 investigates the mapping $\mathcal{M}_A : \eta_{\text{m}} \rightarrow \tilde{\eta}$, where fully resolved wave surfaces are reconstructed from sparse buoy measurements. We assume, five buoys are positioned equidistantly within the region unaffected by the Tukey window tapering (see Sec. II C 2), resulting in positions $x_{\text{b}} = \{488.76, 731.18, 973.61, 1216.03, 1462.37\}$ m. The PINO configuration is derived from a hyperparameter study (appendix Tab. I) and employs $n_t = 3$ Fourier layers, $n_{\text{m}} = 128$ modes, and a latent width of $n_{\text{w}} = 32$. The model \mathcal{M}_A achieved minimum validation loss after 52 epochs, and the corresponding model weights are reloaded and used for evaluation on the test set.

Figure 3 illustrates the performance of the trained PINO \mathcal{M}_A for one representative test set sample (no. 133, $L_{\text{p}} = 150$ m and $\varepsilon = 0.05$). The upper left panel shows the five sparse input buoy measurements η_{m} from a top-down view, restricted to the region unaffected by Tukey window tapering. The subsequent panel displays the wave surface $\tilde{\eta}$ reconstructed by \mathcal{M}_A in only 0.014 s. It is followed by the fully

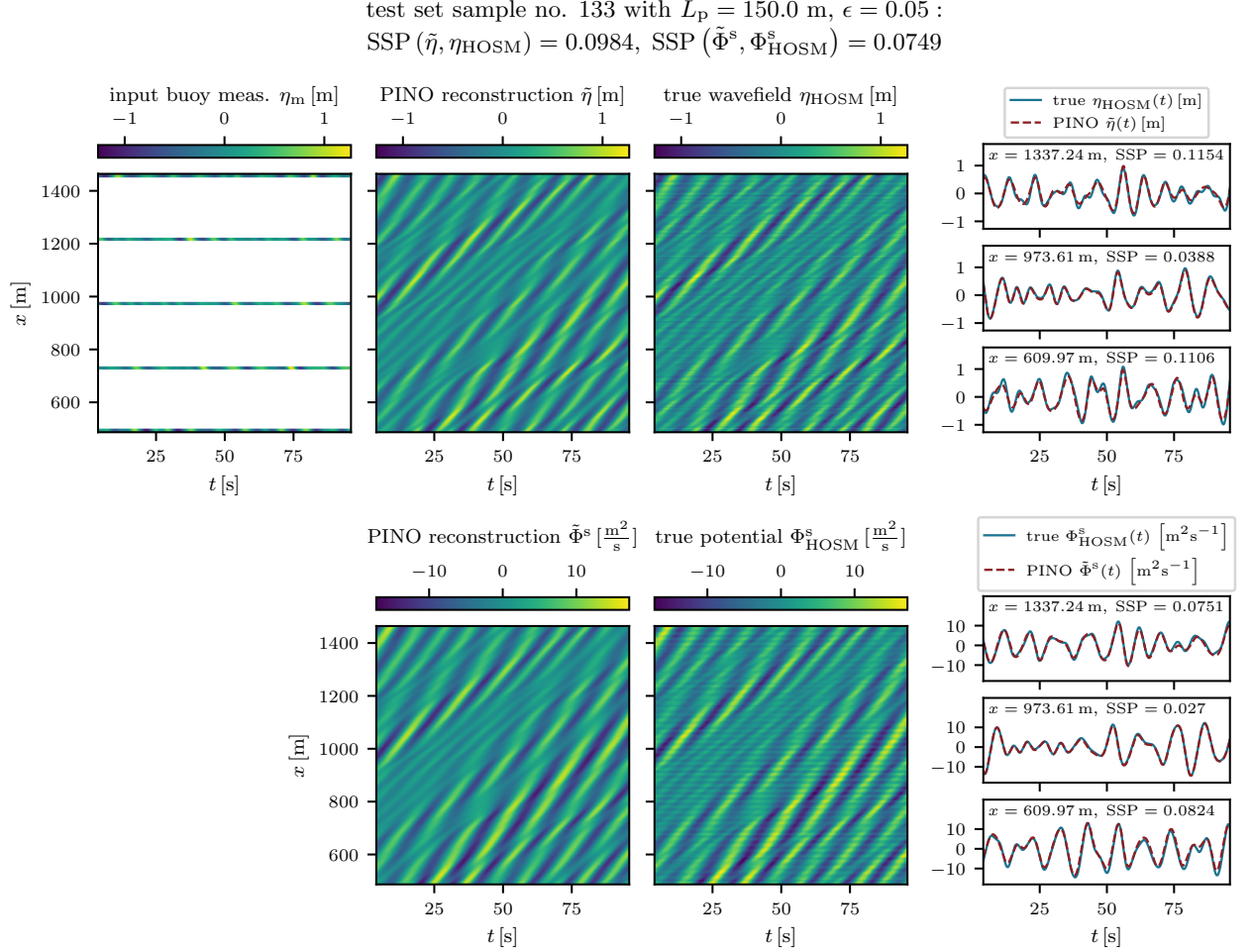


FIG. 3. Reconstruction of the fully resolved wave surface $\tilde{\eta}$ and surface velocity potential $\tilde{\Phi}^s$ from five sparse buoy measurements η_m using the PINO model (\mathcal{M}_A) for one test set sample. In the upper panels, $\tilde{\eta}$ and the reference surface η_{HOSM} show a good agreement. The same applies for $\tilde{\Phi}^s$ and Φ_{HOSM}^s in the lower panels. Notably, reconstructions were achieved without access to fully resolved data during training of \mathcal{M}_A - the model relies solely on the physics-based loss for reconstruction between buoys.

resolved reference η_{HOSM} , which is available only due to the synthetic nature of our data. Although never used during training, these references enable quantitative post-training validation of our developed method. From this, we observe that the reconstruction closely matches the reference, with a low error of SSP = 0.0984. In the right panel, cross-sections at three spatial locations further confirm the accuracy: the central slice, which is aligned with a measurement location, shows near-perfect agreement between $\tilde{\eta}$ and η_{HOSM} . Also the off-center slices, which are in between two measurement points, reveal only minor discrepancies in small-scale features, while the more relevant wave crests and troughs are largely well reconstructed. The bottom row of Fig. 3 presents the simultaneously reconstructed surface velocity potential $\tilde{\Phi}^s$ which also shows high agreement to its reference Φ_{HOSM}^s , as reflected by a SSP = 0.0749.

After evaluating this individual sample, the performance of PINO \mathcal{M}_A on the entire test set is assessed, which contains 210 additional buoy measurements with different L_p -

and ϵ -values, and random phases. This analysis is summarized in Fig. 4, where each cell represents the mean SSP for a specific L_p - ϵ -combination, while the mean SSP across all test samples is 0.1035. The figure illustrates that reconstruction accuracy slightly improves for wavefields with lower steepness (ϵ) or longer peak wavelengths (L_p). This observation may be attributed to multiple factors: (1) Steeper, higher waves inherently exhibit stronger nonlinearities, complicating the reconstruction. (2) Samples for higher wave heights include smaller-scale wave components, as we are considering highly realistic sea states. This results in an underrepresentation of higher wave components in the training data, reducing model performance for high- ϵ samples. (3) Waves with shorter L_p may be more difficult to reconstruct due to the fixed buoy spacing of $\Delta x_b \approx 246$ m. While the longest waves in the dataset travel just slightly over one peak wavelength between measurement points, shorter waves undergo more rapid spatial variation between buoys. As a result, some features of short waves may be lost, leading to reduced reconstruction

accuracy. However, since we aim for a model that is transferable to real ocean conditions, we must assume a uniform buoy spacing for all wavelengths. Nevertheless, even for short L_p and high ϵ , the reconstruction errors remain within a satisfactory range, so that it can still be concluded that model \mathcal{M}_A is capable of successfully generalizing its reconstruction capability across a range of wave conditions.

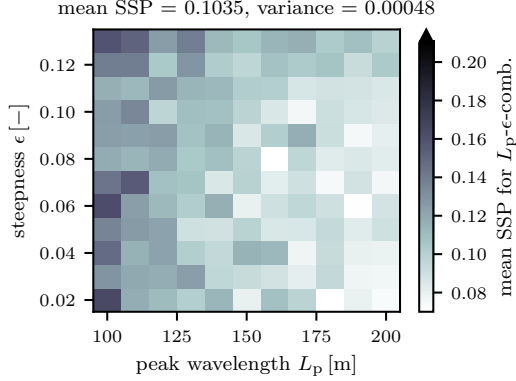


FIG. 4. Mean wave surface reconstruction error SSP ($\tilde{\eta}, \eta_{\text{HOSM}}$) across the test set using PINO \mathcal{M}_A with buoy input data. Each cell shows the average SSP error for a specific combination of peak wavelength (L_p) and wave steepness (ϵ). Comparatively low errors are observed for longer L_p and lower ϵ , while accuracy remains satisfactory even for challenging parameter combinations.

Overall, the results presented in Fig. 3 provide strong evidence in support of hypothesis (H1a), as the PINO \mathcal{M}_A successfully reconstructs spatio-temporal wave surfaces from sparse buoy measurements. Notably, ground truth data (η_{HOSM} and Φ_{HOSM}^s) is used exclusively for post-training evaluation in this academic setting, and is not required during training. This directly supports hypothesis (H2), as the physics-informed training approach would enable learning from sparse, real-world buoy measurements, where high-resolution reference data is typically unavailable. This presents a situation where supervised learning is not applicable. Furthermore, the PINO \mathcal{M}_A achieves a reconstruction time of approximately 0.014 s per sample on the utilized standard workstation, which is comparable to the method of Köllisch et al. (2018)¹³. This rapid inference highlights the suitability of \mathcal{M}_A for real-time wavefield prediction after the reconstruction, thereby supporting hypothesis (H3). Finally, as shown in Fig. 4, the PINO \mathcal{M}_A demonstrates generalization across a broad range of wave conditions - a capability that standard PINN approaches do not achieve. Thus, the findings in this section also support hypothesis (H4).

B. Reconstruction from radar measurements

Building upon the successful reconstruction of wavefields from sparse buoy measurements, we now address case B in Fig. 2, which focuses on reconstructing phase-resolved wave surfaces from radar snapshot data, formally denoted as $\mathcal{M}_B : \xi_m \rightarrow \tilde{\eta}$. Unlike buoy measurements, radar intensities do

not exhibit a direct proportionality to wave elevations, thereby introducing additional complexity to the reconstruction task. To address this, we incorporate a single calibration buoy measurement η_{cal} in the sensor loss term $\mathcal{L}_{\text{sensor}}$, (but not as a direct input) to enable the model to learn the mapping between radar intensity values and wave elevation values. For this task, a slightly modified PINO architecture yielded the best performance in a hyperparameter study (appendix Tab. II). This configuration employs $n_f = 3$ Fourier layers and $n_m = 128$ modes, but a larger latent width of $n_w = 64$, reflecting the increased complexity of the problem arising from the indirect nature of the measurements. The model \mathcal{M}_B achieved its lowest validation loss after 243 epochs, at which point the corresponding weights are reloaded.

For the evaluation of PINO \mathcal{M}_B , we employ the same test set sample (no. 133) as in the previous section. The input sequence of radar intensity snapshots ξ_m is displayed in the left panel of Fig. 5. These snapshots, recorded with $\Delta t_r = 2$ s, reveal certain spatial regions impacted by shadowing modulation, evident as zero-intensities. The same panel also indicates the location of the calibration buoy measurement η_{cal} at $x_b = 973.61$ m, which only serves for calibration purposes of $\mathcal{L}_{\text{sensor}}$ during training but is not required during inference. The adjacent panels present the reconstructed wave surface $\tilde{\eta}$ and the corresponding reference field η_{HOSM} . As in the previous case, reference fields in this form were not available during training. Although the reconstruction error (SSP = 0.1090) is marginally higher than in case A, the reconstruction $\tilde{\eta}$ demonstrates strong agreement with the reference η_{HOSM} , as further confirmed by the cross-sections in the right panel. Similar accuracy is observed for the surface velocity potential in the lower panels, where the PINO reconstruction $\tilde{\Phi}^s$ achieves a SSP = 0.0949 relative to the reference Φ_{HOSM}^s .

As shown in Fig. 6, the average reconstruction error for wave surfaces from radar measurements across the entire test dataset is SSP = 0.1341, which is higher than the error observed for buoy-based reconstructions (SSP = 0.1035; see Fig. 4), but remains within an satisfying range. As before, each cell of the figure represents the mean SSP for all test set samples corresponding to a specific L_p - ϵ parameter combination. Notably, in contrast to the previous section, samples with higher steepness now exhibit a more pronounced increase in reconstruction error. This increase cannot be attributed solely to wave nonlinearity or the underrepresentation of higher wave components in the training data, as was previously discussed. Instead, it is primarily a consequence of geometric shadowing modulation effects: samples with higher steepness are more severely affected by shadowing modulation, resulting in radar measurements that inherently contain less information, making the reconstruction task more challenging for these cases.

This relationship between reduced information density in the radar input ξ_m and increased reconstruction errors is further illustrated in Fig. 7, which presents results for another test set sample (no. 173) characterized by $L_p = 150$ m and the maximum steepness $\epsilon = 0.13$. The left panel shows that a significantly larger portion of the input exhibits zero intensity values (in contrast to sample no. 133 with $\epsilon = 0.05$ in Fig. 5).

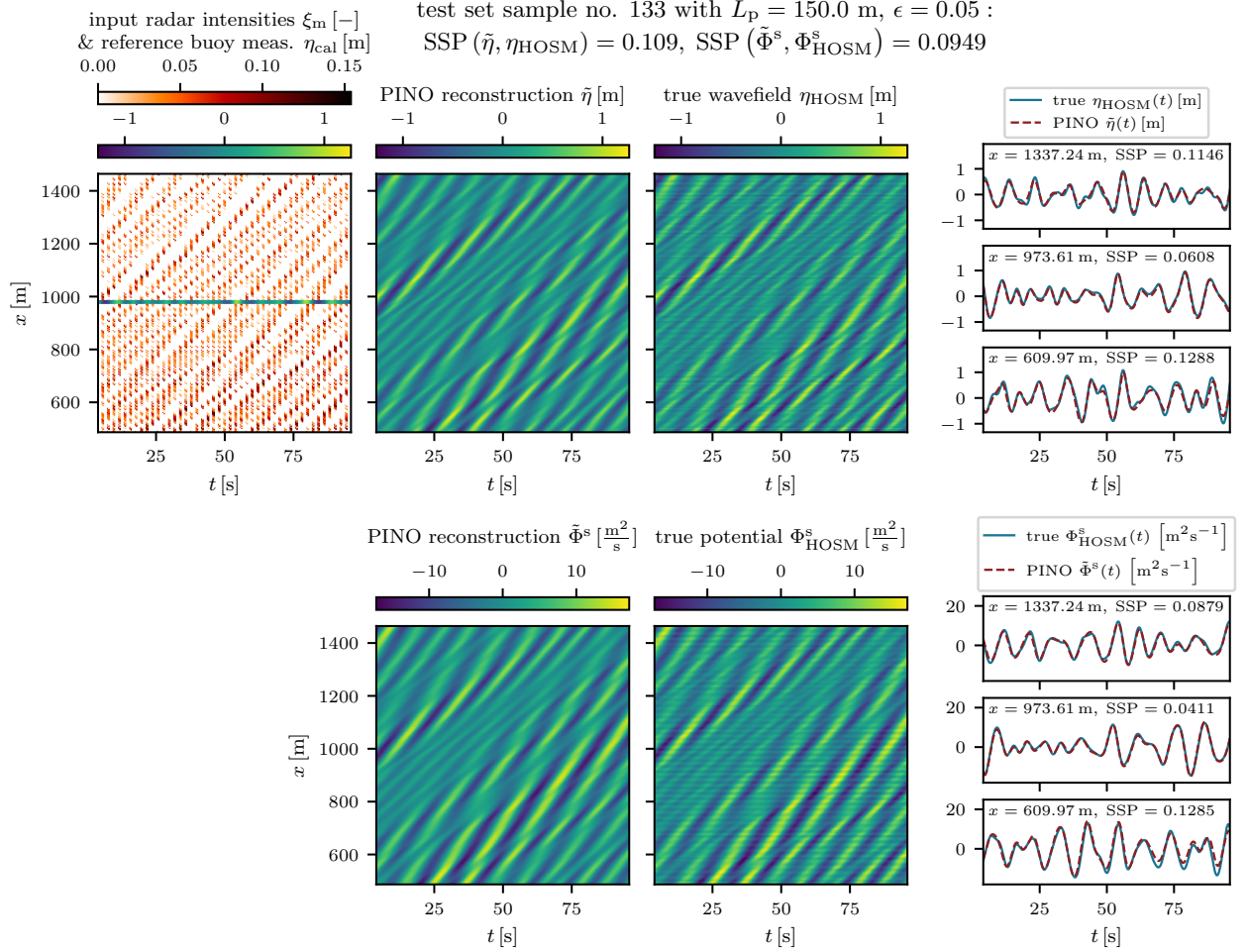


FIG. 5. Reconstruction of a fully resolved wave surface $\tilde{\eta}$ and surface velocity potential $\tilde{\Phi}^s$ from radar snapshot intensities ξ_m using the trained PINO model (\mathcal{M}_B) for the same test sample as in Fig. 3. The radar input snapshots in the left panel (with $\Delta t_r = 2$ s) exhibit regions of zero intensity due to shadowing modulation. The location of the calibration buoy measurement η_{cal} is also indicated. Despite the increased complexity of radar-based reconstruction, that cause a small decrease in accuracy compared to the previous case, $\tilde{\eta}$ and $\tilde{\Phi}^s$ show a satisfying agreement with the references η_{HOSM} and Φ_{HOSM}^s .

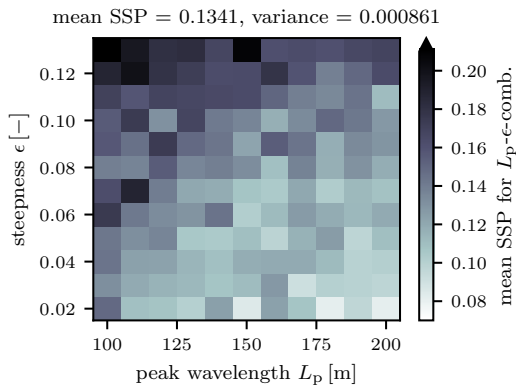
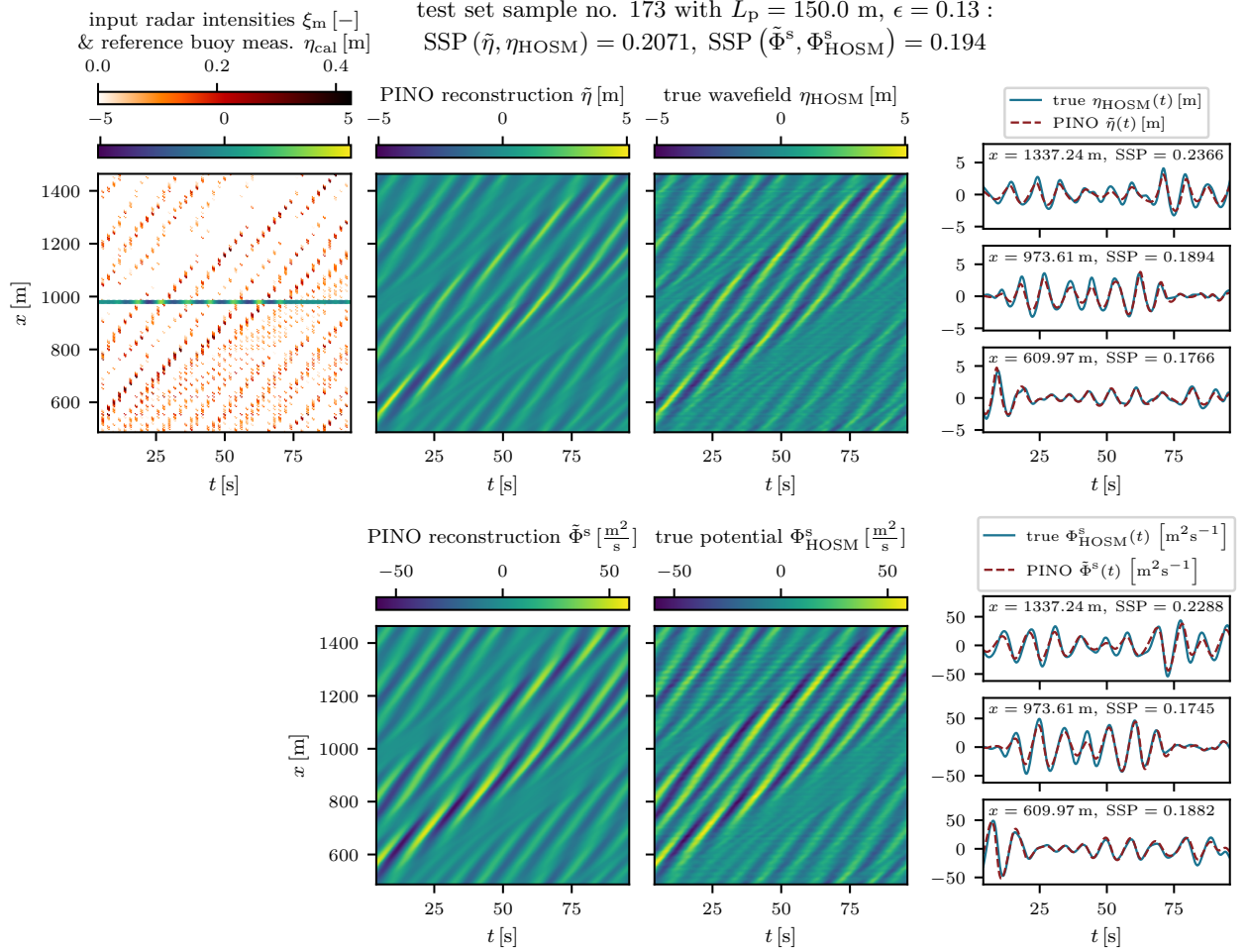


FIG. 6. Mean wave surface reconstruction error SSP ($\tilde{\eta}, \eta_{HOSM}$) across the test set using PINO \mathcal{M}_B with radar snapshot inputs ξ_m . Each cell shows the average SSP error for a specific L_p - ϵ -combination. Compared to buoy-based reconstructions in Fig. 4, errors are generally higher, particularly for samples with high ϵ , due to increased shadowing effects in ξ_m .

This pronounced shadowing effect directly impacts the reconstruction quality of $\tilde{\eta}$, particularly at greater distances from the radar located at $x = 0$ m. This trend is evident in the cross-section at $x = 1337.24$ m, where the SSP is higher compared to the closer cross-section locations. Nevertheless, considering that sample no. 173 exhibits one of the highest reconstruction errors in the entire test dataset, the accuracy of $\tilde{\eta}$ and $\tilde{\Phi}^s$ remains satisfactory when compared to their references. While some wave crests and troughs are not perfectly captured, the phase alignment is highly accurate, and the qualitative agreement in the top-view plots is still acceptable. Moreover, the observation of increased reconstruction errors from radar data for higher ϵ -values is consistent with findings previously reported for the purely supervised approach in Ehlers et al. (2023)²⁵ and can therefore not be attributed to the underlying principle of the PINO approach but is rather a physical issue.



In summary, the results of this section demonstrate that the PINO model \mathcal{M}_B can successfully reconstruct phase-resolved nonlinear wave surfaces from radar snapshot measurements, supporting hypothesis (H1b). While reconstruction errors are higher than for buoy-based inputs in the last section, primarily due to information loss from shadowing modulation for high steepness samples, the accuracy remains robust across a broad range of conditions. As with the buoy case, no ground truth wave fields are needed during training, supporting hypothesis (H2). Moreover, inference times remain suitable for real-time applications (H3). Although the radar-based PINO model (\mathcal{M}_B) does not generalize to a wide range of wave conditions as effectively as the buoy-based model (\mathcal{M}_A), its limitations are primarily caused by the lower information content and measurement artefacts present in radar data, rather than by the model architecture itself. Notably, the generalisation performance of \mathcal{M}_B still remains substantially better than that of conventional PINN methods, which show no generalization

capability at all. Therefore, despite the challenges posed by radar measurements, hypothesis (H4) is still supported, confirming the potential of PINOs for practical wavefield monitoring using diverse sensor types.

IV. CONCLUSION AND OUTLOOK

In this study, we presented a Physics-Informed Neural Operator (PINO) tailored for wave data assimilation. Our PINO reconstructs fully-resolved free-surface wave elevation fields and corresponding velocity potential fields from sparse measurements, such as buoy data (case A) or radar snapshots combined with data from a single calibration buoy (case B). A key advantage of our approach is that it eliminates the need for fully-resolved ground-truth data during training, which is typically impractical to obtain in real-ocean applications. This implies, instead of directly minimizing the reconstruction er-

ror relative to a ground truth, as in conventional supervised learning, the PINO learns to generate physically consistent wave fields by minimizing residuals of the governing equations. Specifically, we incorporate the residuals of the free-surface boundary conditions, derived from the potential flow theory of ocean gravity waves, directly into the loss function. These physics-based constraints guide the model to infer consistent wave fields between sparsely distributed measurement locations.

Compared to our previous methods for wave surface reconstruction, the proposed PINO combines the strengths of our FNO-based approach²⁵ and PINN-based approach²⁷, while addressing their limitations. First, the PINO is highly data-efficient as a training set of only 634 sparse input samples is enough to achieve a satisfying performance on the test set, quantified by mean SSP values of $SSP = 0.1035$ (case A) and $SSP = 0.1341$ (case B). This demonstrates that embedding physical knowledge significantly reduces the amount of data required, compared to conventional machine learning models such as our FNO-approach²⁵, which needed approximately three times more training data to reach similar accuracy. Moreover, unlike the FNO²⁵, the PINO does not rely on labelled datasets of ground-truth wave elevations, making it directly applicable in real-world scenarios with only sparse observational data. In contrast to our PINN-approach²⁷, the PINO can assimilate indirect measurements such as radar backscatter and does not require a time-consuming solution of a separate inverse problem for each wave instance. Instead, once trained, the PINO generalizes across wave conditions and enables rapid, instance-independent inference, taking by far less than one second to reconstruct a previously unseen wave instance. Overall, these properties make the proposed PINO approach a promising candidate for real-time, physics-constrained wave field reconstruction from sparse and indirect measurements, with high potential for operational application in engineering and oceanography.

Currently, the proposed PINO approach has been demonstrated on long-crested, unidirectional ($1D + t$) wave surfaces. Extending this framework to realistic two-dimensional ($2D + t$) wave fields, where waves arrive from multiple directions and interact through complex superposition, is the future perspective for this work. Since the core of the PINO relies on Fourier layers that can be extended to higher dimensions, this extension does not present fundamental methodological challenges. However, the increased dimensionality will demand substantially more computational resources or efficient parallelization strategies. Although the more complex wave fields may slightly reduce reconstruction accuracy, we expect that the embedded physics constraints will sustain robust performance. Importantly, once trained, the PINO should still enable extremely fast inference, making real-time physics-informed wave field reconstruction in $2D + t$ scenarios feasible for practical applications.

FUNDING

This work was supported by the Deutsche Forschungsgemeinschaft (DFG - German Research Foundation) [project number 277972093: Excitability of Ocean Rogue Waves].

DECLARATION OF INTERESTS

The authors declare that they have no known competing financial interests or personal relationships that could have appeared to influence the work reported in this paper.

DECLARATION OF GENERATIVE AI AND AI- ASSISTED TECHNOLOGIES IN THE WRITING PROCESS

The investigations were conducted and the manuscript was written completely by the authors. Once the manuscript was completed, the authors used ChatGPT 3.5 (<https://chat.openai.com/>) in order to improve its grammar and readability. After using this tool, the authors reviewed and edited the content as needed and take full responsibility for the content of the publication.

DATA AVAILABILITY STATEMENT

The data that supports the findings of this study are available from the corresponding author upon reasonable request.

Appendix A: Hyperparameter study

To identify the optimal configuration for the PINO architecture shown in Fig. 2, a hyperparameter study was conducted for both, case A (reconstruction of wave elevations $\tilde{\eta}$ from buoy measurements η_m) and case B (reconstruction of wave fields $\tilde{\eta}$ from radar snapshots ξ_m). In this hyperparameter study, the number of FNO layers n_F , the number of Fourier modes retained without truncation n_m , and the width of the latent representation n_w , were systematically varied. Additionally, the total number of resulting weights from all layers ($I, P, R_{L_i}, W_{L_i}, Q$) are counted.

Table I clearly shows that for case A, a configuration with $n_F = 3$, $n_m = 128$ and $n_w = 32$ performed best, achieving the lowest loss \mathcal{L} and SSP values on the validation set. Additionally, the variance of the SSP values for this configuration was among the lowest.

In contrast, for case B in Table II, due to the increased complexity of radar-based reconstructions, the best results were achieved with a larger latent dimension $n_w = 64$, while maintaining $n_F = 3$ and $n_m = 128$.

For the rows in both tables marked with an underscore (-), training with a batch size of 8 was not possible on the available hardware (NVIDIA GeForce RTX 3090 GPU). However, it can be expected that even better reconstruction results could be achieved with more powerful hardware.

TABLE I. Results of the hyperparameter study for the PINO architecture for the reconstruction of wave fields from buoy measurements ($\mathcal{M}_A : \eta_m \rightarrow \tilde{\eta}$) in Sec. III A. Each investigated architecture is characterized by several Fourier layers n_F , a width of the latent representation n_w and the modes n_m for truncation of the layers' Fourier series.

PINO hyperparameters						loss \mathcal{L}		SSP		
layers n_F	modes n_m	width n_w	#weights	epochs		train	val	train	val	val variance
2	64	16	8,398,521	249		0.04145	0.04466	0.1287	0.1283	0.001061
		32	33,567,993	235		0.03328	0.03885	0.1163	0.1161	0.000824
		48	75,515,705	223		0.03115	0.03724	0.1127	0.1126	0.000746
		64	134,241,657	195		0.02896	0.03646	0.1102	0.1105	0.000703
2	128	16	33,564,345	243		0.03551	0.03956	0.1169	0.1164	0.000718
		32	134,231,289	153		0.03146	0.03850	0.1101	0.1099	0.000586
		48	302,008,121	203		0.02844	0.03635	0.1053	0.1056	0.000503
		64	536,894,841	180		0.02862	0.03567	0.1058	0.1064	0.000511
2	256	16	134,227,641	218		0.03542	0.03984	0.1181	0.1179	0.000743
		32	536,884,473	193		0.02948	0.03725	0.1073	0.1073	0.000562
		48	1,207,977,785	-		-	-	-	-	-
		64	2,147,507,577	-		-	-	-	-	-
3	64	16	12,593,097	208		0.03194	0.03898	0.1139	0.1141	0.000810
		32	50,346,265	84		0.02856	0.03841	0.1089	0.1093	0.000706
		48	113,266,793	50		0.03082	0.03730	0.1111	0.1112	0.000729
		64	201,354,681	77		0.02854	0.03710	0.1086	0.1089	0.000680
3	128	16	50,341,833	84		0.03151	0.03911	0.1087	0.1084	0.000593
		32	201,341,209	52		0.02954	0.03803	0.1048	0.1049	0.000501
		48	453,005,417	52		0.03038	0.03731	0.1063	0.1059	0.000501
		64	805,334,457	50		0.03129	0.03675	0.1065	0.1068	0.000520
3	256	16	201,336,777	76		0.03006	0.03844	0.1065	0.1073	0.000544
		32	805,320,985	50		0.02993	0.03715	0.1060	0.1058	0.000534
		48	1,811,959,913	-		-	-	-	-	-
		64	3,221,253,561	-		-	-	-	-	-
4	64	16	16,787,673	76		0.03033	0.04025	0.1121	0.1135	0.000801
		32	67,124,537	54		0.02636	0.03933	0.1069	0.1079	0.000689
		48	151,017,881	50		0.02859	0.03688	0.1081	0.1085	0.000677
		64	268,467,705	51		0.02980	0.03762	0.1087	0.1088	0.000698
4	128	16	67,119,321	50		0.02982	0.03883	0.1054	0.1055	0.000517
		32	268,451,129	26		0.03101	0.03773	0.1053	0.1054	0.000531
		48	604,002,713	30		0.02935	0.03721	0.1045	0.1053	0.000576
		64	1,073,774,073	-		-	-	-	-	-
4	256	16	268,445,913	51		0.02912	0.0384	0.1053	0.1057	0.000498
		32	1,073,757,497	-		-	-	-	-	-
		48	2,415,942,041	-		-	-	-	-	-
		64	4,294,999,545	-		-	-	-	-	-

¹A. P. Engsig-Karup, H. B. Bingham, and O. Lindberg, "An efficient flexible-order model for 3d nonlinear water waves," *Journal of computational physics* **228**, 2100–2118 (2009).

²G. Wu and R. E. Taylor, "Finite element analysis of two-dimensional nonlinear transient water waves," *Applied Ocean Research* **16**, 363–372 (1994).

³Q. Ma and S. Yan, "Quasi ale finite element method for nonlinear water waves," *Journal of computational physics* **212**, 52–72 (2006).

⁴S. T. Grilli, P. Guyenne, and F. Dias, "A fully non-linear model for three-dimensional overturning waves over an arbitrary bottom," *International journal for numerical methods in fluids* **35**, 829–867 (2001).

⁵D. G. Dommermuth and D. K. P. Yue, "A high-order spectral method for the study of nonlinear gravity waves," *Journal of Fluid Mechanics* **184**, 267–288 (1987).

⁶B. J. West, K. A. Brueckner, R. S. Janda, D. M. Milder, and R. L. Milton, "A new numerical method for surface hydrodynamics," *Journal of Geo-*

physical Research: Oceans **92**, 11803–11824 (1987).

⁷G. Wu, *Direct simulation and deterministic prediction of large-scale non-linear ocean wave-field*, Ph.D. thesis, Massachusetts Institute of Technology (2004).

⁸G. Ducrozet, F. Bonnefoy, D. Le Touzé, and P. Ferrant, "3-d hos simulations of extreme waves in open seas," *Natural Hazards and Earth System Sciences* **7**, 109–122 (2007).

⁹G. Ducrozet, F. Bonnefoy, D. Le Touzé, and P. Ferrant, "Hos-ocean: Open-source solver for nonlinear waves in open ocean based on high-order spectral method," *Computer Physics Communications* **203**, 245–254 (2016).

¹⁰F. Bonnefoy, G. Ducrozet, D. Le Touzé, and P. Ferrant, "Time domain simulation of nonlinear water waves using spectral methods," in *Advances in numerical simulation of nonlinear water waves* (World Scientific, 2010) pp. 129–164.

¹¹M. Klein, M. Dudek, G. F. Clauss, S. Ehlers, J. Behrendt, N. Hoffmann,

TABLE II. Results of the hyperparameter study for the PINO architecture for the reconstruction of wave fields from radar snapshot measurements ($\mathcal{M}_B : \xi_m \rightarrow \hat{\eta}$) in Sec. III B. Each investigated architecture is characterized by several Fourier layers n_F , a width of the latent representation n_w and the modes n_m for truncation of the layers' Fourier series.

PINO hyperparameters					loss \mathcal{L}		SSP		
layers n_F	modes n_m	width n_w	#weights	epochs	train	val	train	val	val variance
2	64	16	8,421,021	248	0.05935	0.08450	0.1779	0.1803	0.001837
		32	33,590,493	244	0.03649	0.07329	0.1690	0.1712	0.001609
		48	75,538,205	201	0.02511	0.07818	0.1624	0.1652	0.001520
		64	134,264,157	98	0.03036	0.08295	0.1607	0.1645	0.001457
2	128	16	33,586,845	243	0.03419	0.06904	0.1543	0.1571	0.001569
		32	134,253,789	247	0.01717	0.05807	0.1541	0.1564	0.001376
		48	302,030,621	246	0.01412	0.05522	0.1497	0.1522	0.001173
		64	536,917,341	246	0.01373	0.05618	0.1454	0.1480	0.001126
2	256	16	134,250,141	249	0.02234	0.07399	0.1522	0.1547	0.001295
		32	536,906,973	245	0.01793	0.06739	0.1654	0.1678	0.001551
		48	-	-	-	-	-	-	-
		64	-	-	-	-	-	-	-
3	64	16	12,615,597	247	0.03124	0.06374	0.1707	0.1727	0.001360
		32	50,368,765	197	0.01399	0.06040	0.1553	0.1579	0.001136
		48	113,289,293	242	0.01360	0.07132	0.1507	0.1542	0.001276
		64	201,377,181	241	0.01179	0.06978	0.1514	0.1548	0.001226
3	128	16	50,364,333	249	0.01649	0.04941	0.1465	0.1496	0.001276
		32	201,363,709	238	0.01096	0.04317	0.1400	0.1425	0.001052
		48	453,027,917	246	0.01032	0.04543	0.1401	0.1428	0.001071
		64	805,356,957	243	0.00950	0.04437	0.1343	0.1369	0.000920
3	256	16	201,359,277	243	0.01431	0.05628	0.1508	0.1537	0.001287
		32	805,343,485	248	0.00934	0.03932	0.1437	0.1456	0.000839
		48	-	-	-	-	-	-	-
		64	-	-	-	-	-	-	-
4	64	16	16,810,173	235	0.02077	0.05630	0.1806	0.1829	0.001177
		32	67,147,037	97	0.01166	0.05507	0.1598	0.1628	0.001072
		48	151,040,381	224	0.00846	0.05519	0.1638	0.1670	0.001214
		64	268,490,205	121	0.00895	0.05676	0.1628	0.1671	0.00127
4	128	16	67,141,821	248	0.01001	0.04011	0.1412	0.1446	0.001013
		32	268,473,629	239	0.00804	0.03744	0.1504	0.1529	0.000922
		48	-	-	-	-	-	-	-
		64	-	-	-	-	-	-	-
4	256	16	268,468,413	249	0.00915	0.03916	0.1478	0.1506	0.000837
		32	-	-	-	-	-	-	-
		48	-	-	-	-	-	-	-
		64	-	-	-	-	-	-	-

and M. Onorato, "On the deterministic prediction of water waves," *Fluids* **5** (2020), 10.3390/fluids5010009.

¹²G. Ducrozet, H. B. Bingham, A. P. Engsig-Karup, F. Bonnefoy, and P. Ferrant, "A comparative study of two fast nonlinear free-surface water wave models," *International Journal for Numerical Methods in Fluids* **69**, 1818–1834 (2012).

¹³N. Köllisch, J. Behrendt, M. Klein, and N. Hoffmann, "Nonlinear real time prediction of ocean surface waves," *Ocean Engineering* **157**, 387–400 (2018).

¹⁴T. Hlophé, *Efficient real-time deterministic wave prediction for marine renewable energy*, Ph.D. thesis, The University of Western Australia (2023).

¹⁵S. Yoon, J. Kim, and W. Choi, "An explicit data assimilation scheme for a nonlinear wave prediction model based on a pseudo-spectral method," *IEEE Journal of Oceanic Engineering* **41**, 112–122 (2016).

¹⁶G. Wang and Y. Pan, "Phase-resolved ocean wave forecast with ensemble-

based data assimilation," *Journal of Fluid Mechanics* **918**, A19 (2021).

¹⁷E. Blondel, F. Bonnefoy, and P. Ferrant, "Deterministic non-linear wave prediction using probe data," *Ocean Engineering* **37**, 913–926 (2010).

¹⁸S. Aragh and O. Nwogu, "Variation assimilating of synthetic radar data into a pseudo-spectral wave model," *Journal of Coastal Research*, 235–244 (2008).

¹⁹Y. Qi, G. Wu, Y. Liu, M.-H. Kim, and D. K. P. Yue, "Nonlinear phase-resolved reconstruction of irregular water waves," *Journal of Fluid Mechanics* **838**, 544–572 (2018).

²⁰W. Fujimoto and T. Waseda, "Ensemble-based variational method for nonlinear inversion of surface gravity waves," *Journal of Atmospheric and Oceanic Technology* **37**, 17–31 (2020).

²¹J. Wu, X. Hao, and L. Shen, "An improved adjoint-based ocean wave reconstruction and prediction method," *Flow* **2**, E2 (2022).

²²*Reconstruction of Ocean Surfaces From Randomly Distributed Measure-*

- ments Using a Grid-Based Method*, International Conference on Offshore Mechanics and Arctic Engineering, Vol. Volume 6: Ocean Engineering (2021).
- ²³N. Desmars, M. Hartmann, J. Behrendt, N. Hoffmann, and M. Klein, "Nonlinear deterministic reconstruction and prediction of remotely measured ocean surface waves," *Journal of Fluid Mechanics* **975**, A8 (2023).
 - ²⁴N. Desmars, *Real-time reconstruction and prediction of ocean wave fields from remote optical measurements*, Theses, École centrale de Nantes (2020).
 - ²⁵S. Ehlers, M. Klein, A. Heinlein, M. Wedler, N. Desmars, N. Hoffmann, and M. Stender, "Machine learning for phase-resolved reconstruction of nonlinear ocean wave surface elevations from sparse remote sensing data," *Ocean Engineering* **288**, 116059 (2023).
 - ²⁶Z. Li, N. Kovachki, K. Azizzadenesheli, B. Liu, K. Bhattacharya, A. Stuart, and A. Anandkumar, "Fourier neural operator for parametric partial differential equations," arXiv preprint arXiv:2010.08895 (2020).
 - ²⁷S. Ehlers, N. Hoffmann, T. Tang, A. H. Callaghan, R. Cao, E. M. Padilla, Y. Fang, and M. Stender, "Physics-informed neural networks for phase-resolved data assimilation and prediction of nonlinear ocean waves," *Physical Review Fluids* (2025).
 - ²⁸M. Raissi, P. Perdikaris, and G. Karniadakis, "Physics-informed neural networks: A deep learning framework for solving forward and inverse problems involving nonlinear partial differential equations," *Journal of Computational Physics* **378**, 686–707 (2019).
 - ²⁹Y. Law, H. Santo, K. Lim, and E. Chan, "Deterministic wave prediction for unidirectional sea-states in real-time using artificial neural network," *Ocean Engineering* **195**, 106722 (2020).
 - ³⁰J. Zhang, X. Zhao, S. Jin, and D. Greaves, "Phase-resolved real-time ocean wave prediction with quantified uncertainty based on variational bayesian machine learning," *Applied Energy* **324**, 119711 (2022).
 - ³¹T. Le Quang, M. H. Dao, and X. Lu, "Prediction of near-field unidirectional and multi-directional random waves from far-field measurements with artificial neural networks," *Ocean Engineering* **278**, 114307 (2023).
 - ³²Y. Liu, X. Zhang, G. Chen, Q. Dong, X. Guo, X. Tian, W. Lu, and T. Peng, "Deterministic wave prediction model for irregular long-crested waves with recurrent neural network," *Journal of Ocean Engineering and Science* **9**, 251–263 (2024).
 - ³³F. Mohaghegh, J. Murthy, and M.-R. Alam, "Rapid phase-resolved prediction of nonlinear dispersive waves using machine learning," *Applied Ocean Research* **117**, 102920 (2021).
 - ³⁴M. Wedler, M. Stender, M. Klein, and N. Hoffmann, "Machine learning simulation of one-dimensional deterministic water wave propagation," *Ocean Engineering* **284**, 115222 (2023).
 - ³⁵Z. Li, H. Zheng, N. Kovachki, D. Jin, H. Chen, B. Liu, K. Azizzadenesheli, and A. Anandkumar, "Physics-informed neural operator for learning partial differential equations," *ACM / IMS J. Data Sci.* **1** (2024), 10.1145/3648506.
 - ³⁶S. G. Rosofsky, H. Al Majed, and E. A. Huerta, "Applications of physics informed neural operators," *Machine Learning: Science and Technology* **4**, 025022 (2023).
 - ³⁷S. Zhao, Z. Li, B. Fan, Y. Wang, H. Yang, and J. Wang, "Lesnets (large-eddy simulation nets): Physics-informed neural operator for large-eddy simulation of turbulence," (2024), arXiv:2411.04502 [physics.flu-dyn].
 - ³⁸T. Konuk and J. Shragge, "Physics-guided deep learning using fourier neural operators for solving the acoustic vti wave equation," in *82nd EAGE annual conference & exhibition*, 1 (European Association of Geoscientists & Engineers, 2021) pp. 1–5.
 - ³⁹Q. Wang, L. Jiang, L. Yan, X. He, J. Feng, W. Pan, and B. Luo, "Chaotic time series prediction based on physics-informed neural operator," *Chaos, Solitons & Fractals* **186**, 115326 (2024).
 - ⁴⁰T. Chen and H. Chen, "Universal approximation to nonlinear operators by neural networks with arbitrary activation functions and its application to dynamical systems," *IEEE transactions on neural networks* **6**, 911–917 (1995).
 - ⁴¹C. M. Chiang, M. Stiassnie, and D. K.-P. Yue, *Theory and Applications of Ocean Surface Waves* (World Scientific, 2005) <https://www.worldscientific.com/doi/pdf/10.1142/5566>.
 - ⁴²V. E. Zakharov, "Stability of periodic waves of finite amplitude on the surface of a deep fluid," *Journal of Applied Mechanics and Technical Physics* **9**, 190–194 (1968).
 - ⁴³H. Lünser, M. Hartmann, N. Desmars, J. Behrendt, N. Hoffmann, and M. Klein, "The influence of characteristic sea state parameters on the accuracy of irregular wave field simulations of different complexity," *Fluids* **7** (2022), 10.3390/fluids7070243.
 - ⁴⁴S. P. Neill and M. R. Hashemi, "Chapter 7 - in situ and remote methods for resource characterization," in *Fundamentals of Ocean Renewable Energy*, E-Business Solutions, edited by S. P. Neill and M. R. Hashemi (Academic Press, 2018) pp. 157–191.
 - ⁴⁵G. R. Valenzuela, "Theories for the interaction of electromagnetic and oceanic waves — A review," *Boundary-Layer Meteorology* **13**, 61–85 (1978).
 - ⁴⁶H. Dankert and W. Rosenthal, "Ocean surface determination from x-band radar-image sequences," *Journal of Geophysical Research: Oceans* **109** (2004), 10.1029/2003JC002130.
 - ⁴⁷J. N. Borge, G. R. Rodríguez, K. Hessner, and P. I. González, "Inversion of marine radar images for surface wave analysis," *Journal of Atmospheric and Oceanic Technology* **21**, 1291 – 1300 (2004).
 - ⁴⁸S. Salcedo-Sanz, J. Nieto Borge, L. Carro-Calvo, L. Cuadra, K. Hessner, and E. Alexandre, "Significant wave height estimation using svr algorithms and shadowing information from simulated and real measured x-band radar images of the sea surface," *Ocean Engineering* **101**, 244–253 (2015).
 - ⁴⁹K. Hasselmann, T. Barnett, E. Bouws, H. Carlson, D. Cartwright, K. Enke, J. Ewing, H. Gienapp, D. Hasselmann, P. Kruseman, A. Meerburg, P. Müller, D. Olbers, K. Richter, W. Sell, and H. Walden, "Measurements of wind-wave growth and swell decay during the joint north sea wave project (jonswap)," *Ergänzung zur Deutschen Hydrographischen Zeitschrift, Reihe A (8)* **12**, 1–95 (1973).
 - ⁵⁰E. Bouws, H. Günther, W. Rosenthal, and C. L. Vincent, "Similarity of the wind wave spectrum in finite depth water: 1. spectral form," *Journal of Geophysical Research* **90**, 975–986 (1985).
 - ⁵¹Z. Chen, V. Badrinarayanan, C.-Y. Lee, and A. Rabinovich, "Gradnorm: Gradient normalization for adaptive loss balancing in deep multitask networks," (2018), arXiv:1711.02257 [cs.CV].
 - ⁵²A. A. Heydari, C. A. Thompson, and A. Mehmood, "Softadapt: Techniques for adaptive loss weighting of neural networks with multi-part loss functions," (2019), arXiv:1912.12355 [cs.LG].
 - ⁵³S. Wang, Y. Teng, and P. Perdikaris, "Understanding and mitigating gradient pathologies in physics-informed neural networks," (2020), 2001.04536.
 - ⁵⁴R. Bischof and M. Kraus, "Multi-objective loss balancing for physics-informed deep learning," *ArXiv abs/2110.09813* (2021).
 - ⁵⁵D. P. Kingma and J. Ba, "Adam: A method for stochastic optimization," (2017), arXiv:1412.6980 [cs.LG].
 - ⁵⁶I. Loshchilov and F. Hutter, "Decoupled weight decay regularization," (2019), arXiv:1711.05101 [cs.LG].
 - ⁵⁷M. Perlin and M. Bustamante, "A robust quantitative comparison criterion of two signals based on the sobolev norm of their difference," *Journal of Engineering Mathematics* **101**, 115–124 (2016).
 - ⁵⁸I.-C. Kim, G. Ducrozet, F. Bonnefoy, V. Leroy, and Y. Perignon, "Real-time phase-resolved ocean wave prediction in directional wave fields: Enhanced algorithm and experimental validation," *Ocean Engineering* **276**, 114212 (2023).
 - ⁵⁹A. Dermatis, M. Lasbleis, S. Kim, G. De Hauteclouque, B. Bouscasse, and G. Ducrozet, "A multi-fidelity approach for the evaluation of extreme wave loads using nonlinear response-conditioned waves," *Ocean Engineering* **316**, 119919 (2025).
 - ⁶⁰S. van Essen, "Influence of wave variability on ship response during deterministically repeated seakeeping tests at forward speed," in *Practical Design of Ships and Other Floating Structures*, edited by T. Okada, K. Suzuki, and Y. Kawamura (Springer Singapore, Singapore, 2021) pp. 899–925.